Air-Breathing Bio-cathodes Based on Electro-Active Biochar

from Pyrolysis of Giant Cane Stalks

S. Marzorati[a], A. Goglio[a], S. Fest-Santini[b], D. Mombelli[c], F. Villa[d], P. Cristiani[e], A. Schievano[a,*]

[a] e-Bio Center, Department of Environmental Science and Policy, Università degli Studi di Milano, via Celoria 2, 20133, Milano, Italy

[b] Department of Management, Information and Production Engineering, University of Bergamo, viale Marconi 5, 24044, Dalmine (BG), Italy

[c] Sezione Materiali per Applicazioni Meccaniche, Dipartimento di Meccanica - Politecnico di Milano, via La Masa 1, 20156, Milano, Italy

[d] Department of Food Environmental and Nutritional Sciences, Università degli Studi di Milano, Via Mangiagalli 25, 20133, Milano , Italy

[e] RSE - Ricerca sul Sistema Energetico S.p.A., via Rubattino 54, 20100, Milano, Italy

[*] corresponding author. Email: andrea.schievano@unimi.it, Department of Environmental Science and Policy, Università degli Studi di Milano, via Celoria 2, 20133, Milano, Italy

ABSTRACT

An innovative low-tech solution to fabricate electro-active biochar (*e*-biochar) electrodes for bio-electrochemical systems (BES) is proposed. Ligno-cellulosic stalks of Giant Cane (*Arundo Donax L.*) were subjected to pyrolysis treatment at 900 °C for 1 h. The material kept its original hollow cylindrical shape, rigid morphology and porous texture, as confirmed by 3DX-ray micro-computed tomography. These characteristics are suitable for its use at the air-water interface in BES, as air-breathing bio-cathodes. BET (Brunauer-Emmett-Teller) specific surface area was equal to 114 ± 4 m^2 g^{-1}, with more than 95% of pores in the microporosity range (pore diameter < 1 nm). Surface electrocatalytic activity was sufficient to sustain oxygen reduction reaction at pH 7, in terms of both onset potential (-0.02 V vs Ag/AgCl) and reduction limiting current density (1 A m^{-2}). Electrical resistivity measurements confirmed sufficient conductivity ($8.9 \times 10^{-3} \pm 1 \times 10^{-4}$ Ω m) of the material and Raman spectroscopy allowed to estimate a graphitization degree in relation to the I_D/I_G, equal to 2.26. In parallel, the *e*-biochar were tested as air-exposed bio-cathodes in BES, coupled to carbon cloth bio-anodes. After inoculation with wastewater from swine-farming, current densities were generated in the range of 100-150 mA m^{-2}, along more than 2

months of operation, under sodium acetate feeding. Confocal laser scanning imaging revealed consistent biofilm formation on the water-side surface of the cathodes, while a nearly-complete absence of it at the air-side.

These *e*-biochar electrodes might open innovative perspectives to scale-up BES for different applications. Here, consistent salts depositions on the material after 70 days of exposure to the wastewater, suggest that *e*-biochar biocathodes might serve to recycle nutrients to agricultural soils, through minerals-enriched biochar.

1. INTRODUCTION

Real scale application of bio-electrochemical systems (BES) has been facing the need to find an optimal balance between processes efficiencies and costs. Many researches are addressing to develop low-cost and environmentally-compatible materials to fabricate electrodes for large scale applications, such as wastewater treatment, soil bioremediation, etc. [1–3]. To date, the most competitive materials are based on carbon and include graphite-based rods, fiber brushes and granules, carbon-fiber cloths, carbon paper sheets, carbon felt and reticulated vitreous carbon [1,2,4]. They are selected due to their strong biocompatibility and inert properties at room temperature. The use of such materials as air-breathing cathodes has been coupled to the fabrication of microporous layers, made of activated carbon, pressed on carbon cloths (or other current collector) in the presence of polymeric binders (Nafion, PTFE, etc.) [5,6]. High surface area favors the cathodic oxygen reduction reaction (ORR) that needs the simultaneous presence of solid, liquid and gaseous phases. Microporous layers also act as gas diffusion layer at air-water interface, because the porous structure allows the diffusion of air in contact with the wet surface, impeding water to leak to the air-side [7–9]. Finally, high surface areas promote the formation of electroactive biofilms, able to highly boost a series of cascade reactions towards oxygen reduction which characterize the behavior of aerobic and anaerobic bio-cathode [10,11]. These 'structural' functions is really important for the application of such materials as air-exposed bio-cathodes [11].

However, these composites have some intrinsic limitations for large-scale applications of BES. A major challenge of commercial application of BES is often the high capital cost, especially material cost of anodes, cathodes, and separators. In a literature work [12], the capital cost of the BES was estimated to be around 100 $ m^{-2} for carbon cloth anode and 5000 $ m^{-3} for reactor. Some novel solutions with macroporous hollow fibers were recently proposed [13], still in the field of high-tech materials.

After relatively short time of operation (typically after 1-3 months [14], or 1 year in some optimized case [15]), biofouling and salts deposition phenomena, tend to hinder cathode's performances. Unless restored by specific treatments [16,17], such electrodes should be substituted by new ones. However,

64   these materials are not fully recyclable. Carbon-cloths are based on mixtures of carbon fibers with non-
65   biogenic materials, such as polymeric binders (PTFE, Nafion, etc.). The compactness of the activated
66   carbon mixtures on carbon-cloth electrodes is also guaranteed by the massive presence of water-resistant
67   binders [18,19].

68   In view of environmental large-scale applications of these electrodes, such as wastewater treatment or
69   soil bioremediation, where harvesting electrical power is not the main goal [20,21], avoiding "high-tech",
70   expensive and non-recyclable materials might result in a substantial advantage. An alternative approach
71   should be based on a circular economy concept, where bio-electrodes are fabricated with bio-based and
72   fully-recyclable materials. In this view, biomass-derived charcoal (biochar) represents a class of target
73   materials that would satisfy this purpose. Biochar, the product of biomass thermochemical conversions,
74   has been receiving increasing attention, for several applications. The versatility of biochar depends on its
75   chemical and structural properties. Biochar is often porous and possesses high surface area [22]. Few
76   groups recently started using biochar in BES [23–27], demonstrating its ability of promoting interspecies
77   electron transfer [28]. For example, a variety of biomass-derived biochar (*i.e.* from pomelo peel and wood
78   chips) was recently used in biofilm-driven water treatment processes possessing characteristics of low
79   cost, high specific area, good biocompatibility and moderate electrical conductivity, which basically meet
80   the requirements of biocathode materials [29,30]. In Table 1 some examples of biochar-based electrodes
81   and their main properties is displayed.

82

Biomass source	Pyrolysis temperature / °C	S_{BET} / m^2 g^{-1}	Application	Achieved power density / mW m^{-2}	Reference
Pine wood lumber	1000	183.0	Electrocatalytic support in MFCs	146.7	[30]
Pomelo peel	1000	622.2	ORR electrocatalysis	799	[29]
Pine sawdust pellets	1000	0.04	MFCs electrodes	457	[25]
Bananas	550-900	105.2 - 172.3	MFCs cathode	500	[31]
Chestnut shell	900	468	MFCs anodes	N/A	[32]

83 **Table 1**. Examples of biochars and their characteristics for microbial electrochemical application.

84

85   The fabrication of biochar as base for bio-electrodes, should aim at simultaneously enhancing electrical
86   conductivity, abiotic electrocatalytic properties (*e.g.* ORR), biocompatibility and the capacity to host
87   microbial biofilm communities. These properties would characterize a particular class of biochars. Here,
88   we propose to call it 'electro-active biochar' or '*e*-biochar'. The possibility to obtain *e*-biochar materials
89   with intrinsic structural rigidity, would open the possibility to use them as air-breathing bio-cathodes at

90   the air-water interface, in lieu of microporous layer/gas diffusion layer-based electrodes. Also, the

91   availability of the original biomass in large amounts, at relatively low costs and environmental impacts,

92   would also be a key-factor for success of *e*-biochar in large-scale BES.

93   In a recent experiment, Giant Cane (*Arundo donax L.*) stalks were tested as air-water cylindrical separators,

94   in air-cathode BES [33]. Giant Cane is a wild, perennial plant of emerging interest for sustainable biomass

95   production [34]. In terms of cultivation inputs it is characterized by very low requirements; it easily adapts

96   to a variety of soil and climatic conditions and has been recently considered one of the most promising

97   biomass crops [35]. The plant's stalks, characterized by porous and rigid cylindrical structure, avoided

98   water leaks to the air-side and allowed spontaneous electricity production using an organic-rich

99   wastewater, with carbon-cloth electrodes [33].

100   Here, we fabricate air-breathing bio-cathodes with a rigid cylindrical shape, based on *e*-biochar obtained

101   from controlled pyrolysis of Giant cane stalks. The physico-chemical and electrocatalytic properties were

102   investigated, as well as their performance as air-breathing bio-cathodes in BES aimed at recovering

103   nutrients from wastewater.

104   **2.   MATERIALS AND METHODS**

105   *2.1 Fabrication of e-biochar air-cathodes*

106   Giant Canes were collected in Cascina Marianna (Landriano, PV) from the experimental fields of the

107   Università degli Studi di Milano. Canes with an external homogeneous diameter of 2.5 cm and thickness

108   of about 0.4 cm were selected, cleaned from leaves and cut into cylinders of 15 cm length.

109   The canes were positioned in a quartz tube inside a horizontal furnace (Carbolite) and pyrolized according

110   to the following protocol: 25 min at 25 °C, slow heating (10 °C min^{-1}) up to 900 °C, 1 h held at 900 °C and,

111   finally, cooling down to 25 °C. Some literature methods were taken into account when choosing the

112   optimized temperature and temperature ramp in order to obtain a sufficiently graphitized sample [36–

113   38]. During all the pyrolysis treatment, nitrogen was flowing constantly at 14 NL h^{-1}.

114   Hereafter, 900 °C-pyrolyzed giant cane stalks will be named simply as '*e*-biochar air-cathodes': *e*-BAC.

115   *2.2 Physical-chemical characterization*

116   The Brunauer-Emmett-Teller (BET) specific surface area (SSA) was obtained from N_2 physisorption

117   isotherms at 77 K by an ASAP 2020 (Micrometitics) instrument. Before measurements, sample powders

118   were outgassed at 110 °C for 3 h to remove adsorbed species. SSA value and porosity distribution were

119   determined employing a multipoint BET interpolation of adsorption isotherms and BJH method,
120   respectively.

121   Raman spectra were obtained on a Raman microscope (Micro-Raman Horiba Jobin Yvon HR800 UV)
122   equipped with a CCD camera using 532 nm excitation laser. The acquired spectra were normalized to carry
123   out the curve fitting of the G, D1, D2, D3 and D4 bands. The different bands were adjusted to Voigt type
124   curves, finding the best fit to the experimental data without including the D2 band, as is usual with carbon
125   black samples. The degree of graphitization has been expressed as the ratio of integral intensities of bands
126   G and D1.

127   *2.3 Morphological characterization*

128   Scanning Electron Microscopy (SEM) was performed using a Zeiss SEM EVO 50 microscope.
129   Morphology description and porosity quantification were obtained from X-ray microcomputed
130   tomography. The used microCT unit is based on an open type X-ray source 160 kVp @ 200 µA, a high-
131   precision air-bearing rotating stage and Amorphous Silicon (a-Si) sensor array detector acquiring 16-bit
132   grey level with a pixel matrix of 4096 x 4096 at 100 micrometers. Concerning further technical details of
133   the microCT setup, refer to [39].

134   Fundamentals of tomography are based on the irradiation of a rotating specimen by an X-ray beam and
135   recording the transmitted radiation for different angle steps allowing the 3D reconstruction. 2D grey-scale
136   virtual slices are obtained through retro-projection. Different levels of grey correspond to certain
137   attenuation coefficients, while every voxel represents an exact element of the digitalized object. Through
138   segmentation and further image processing, information related to void space and solid can be extracted.
139   The applicability of this characterization technique depends on the X-ray attenuation (absorption) of the
140   material, which in turn depends on the atomic number of the chemical element, material density and
141   object dimensions. *e*-BAC, like most of biological samples, is expected to be low density material making
142   their 3D morphological inspection in the micrometer scale challenging. Here, this limitation are overcome
143   working with low photon energy and a high dynamic range of the detector: 4000 projections with a
144   resolution of 3.425 µm (calibrated resolution, refer to [39]) acquired at 45 kV, 30 µA and 5300 ms
145   integration time.

146   The global volumetric intensity histogram was expected to be bimodal with peaks referring to the void
147   space and the material matrix. Instead, a further peak was observed having high intensity values whose
148   indicate a high atomic number element. Thereby, a multi-level thresholding method, multi Otsu method,

149   was utilized for the segmentation of the digitalized *e*-BAC volume differencing in voids, *e*-BAC matrix and

150   high X-ray attenuation matter. The latter is a residue of pyrolysis and probably of mineral nature.

151   *2.4 Electrochemical characterizations*

152   Electrical resistivity measurements were performed setting the electrical contacts on opposite ends of the

153   *e*-BACs. A potential scan was performed in the potential window $E = +0.1 / +0.5$ V at a scan rate of 0.010

154     $V\ s^{-1}$. The electrical resistivity ρ was calculated by the equation:

155

$$\rho = R\frac{A}{l}$$

156   Where *R* is the resistance calculated by the slope of the *E vs I* plot, *A* is the area of the section of the

157   *e*-BAC and *l* is the length of the analyzed cylinder. Five different measurements of different sample lengths

158   were performed to ensure the technique reproducibility.

159   Electrochemical active surface area (ECSA) determinations were performed by voltammetric curves

160   recorded in N_2-saturated 100 mM PBS (Phosphate-buffered saline) solution in the double layer region at

161   various scan rates as in previous work by Łukaszewski *et al.* [40]. A three-electrode configuration was

162   used. A weighted piece of *e*-BAC was set as the working electrode, a Pt-wire was the counter electrode

163   and an Ag/AgCl (Amel) in KCl (sat.) was the reference electrode.

164   The specific mass capacitance (C_g) of the electrode was calculated from cyclic voltammograms according

165   to the following equation:

166

$$C_g = \frac{1}{mv(V_c - V_a)} \int_{Va}^{Vc} i(V)dV \qquad (1)$$

167

168   where *C* is the specific capacitance ($F\ g^{-1}$), *m* is the mass (g) of electroactive materials in the electrode, *v*

169   is the potential scan rate ($V\ s^{-1}$), V_c and V_a (V) are the integration limits of the voltammetric curve, and *i(V)*

170   denotes the current density (A) [41].

171   ECSA ($m^2\ g^{-1}$) was then calculated by:

172

$$ECSA = \frac{C_g}{C_{ref}} \qquad (2)$$

173   and compared to the SSA as determined by BET measurements. The chosen reference value of capacity

174   per the unit area [42] used in calculation was $C_{ref} = 9.57\ \mu F\ cm^{-2}$.

175   *2.5 Oxygen reduction reaction (ORR) electrocatalytic activity*

176 Preliminary electrochemical characterization of the cathode was performed in 100 mM PBS solution (pH

177 7.8) by cyclic voltammetry (CV), using a potentiostat (Materials M 510). *e*-BACs were reduced into

178 powders and dispersed in water (10 mg mL^{-1}), sonicated for 5 min and 7 μL were pipetted onto the glassy

179 carbon tip (working electrode, geometric surface area: A = 0.07 cm^2) and dried in a bottom-up position.

180 An electrochemical cell with a graphite counter electrode (Amel 201/S-016) and an Ag/AgCl reference

181 electrode (Amel) in KCl (sat.) was used. Before CV recording, the working electrode was conditioned by

182 cycling in N$_2$ saturated solution within the E = −1.000 / +0.250 V potential range. When using carbonate

183 buffer solution, the potential range was E = −1.2 / +0.1 V. This step was followed by cycling in O$_2$ saturated

184 solution (v = 0.005 V s^{-1}).

185 *2.6 BES assembly and operation*

186 Fig. 1 shows a schematic of the BES experimental setup. The *e*-BACs (rigid carbonaceous cylinders) were

187 sealed on the bottom side, by attaching a polymethyl methacrylate disk with an inert glue (Gomma

188 Liquida, Bostik®) and were ready to be used as hollow-cylindrical cathodes. The *e*-BACs were wrapped by

189 synthetic felt (polyester fibers) as to avoid the short circuit with the anode. The anode was fixed around

190 the external face of the cylinder, by a nylon wire, to completely wrap the cane outside the felt. This system

191 was positioned in a plastic jar, immersed in the electrolyte. To prevent evaporation and oxygen diffusion

192 in the wastewater, the jar was covered by a polystyrene disk, preserving anaerobic conditions, while

193 letting air reach the internal cylindrical *e*-BACs. A plastic net guaranteed the anode's immersion in the

194 electrolyte solution.

195 BES were run in triplicate in batch mode at (25±1) °C. The cell potential difference was recorded every 20

196 min across a proper external load using a multichannel Data Logger (Graphtec midi LOGGER GL820). The

197 generated current (I) was calculated by the Ohm's law ($I = V R^{-1}$, where R is the external resistive load and

198 V is the cell potential difference) and normalized by the cathode's area to obtain the current density (j).

199
200
201
202
203
204
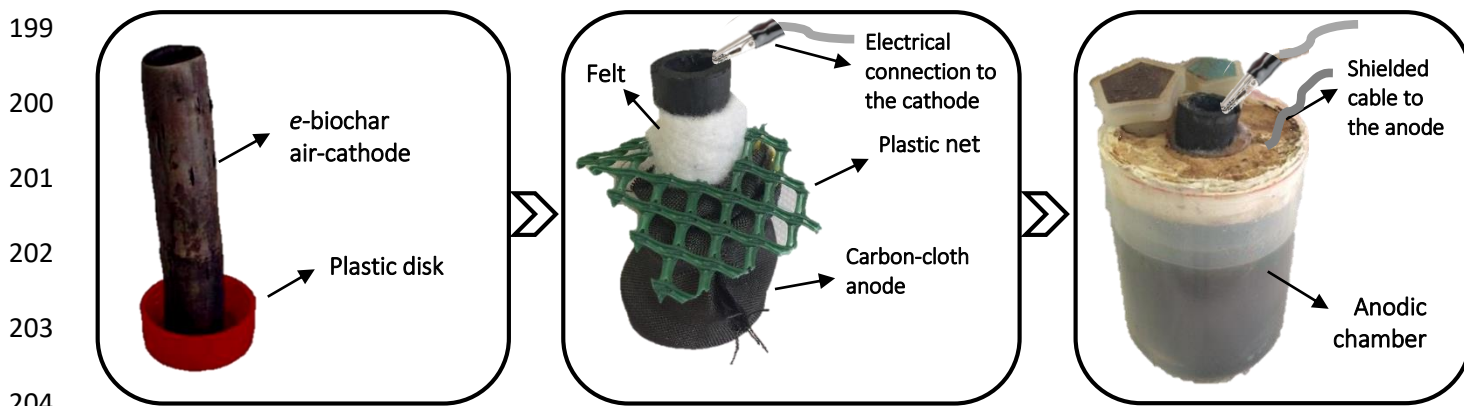
205   **Fig. 1**. Schematic of the BES experimental setup.

206   Anodes were made of plain carbon-cloth (SAATI C1), without any surface treatment. 28 x 9 cm carbon-

207   cloth rectangles were cut and electrically connected to a plastic-insulated copper wire. The electrical

208   connection was then protected by two layers of a bi-component epoxy resin (PROCHIMA COLLA EPOXY).

209   The inoculum was a swine manure collected in a pig-farm near Milan (Italy). Concentrated swine manure

210   (120 mL, COD = 6 g L^{-1}) were added to the anodic chamber at the beginning of the experiment (t=0).

211   Distilled water (0.5 mL) was dropped into the cathodic chamber ensure the cathode's complete wetness

212   and electrolytic contact.

213   After the first decline of the current generated by the system, the anolyte was removed and then refilled

214   by the same amount (120 mL), this time composed half by the same swine manure and half by a synthetic

215   medium. The synthetic medium was chosen according to literature [43,44]. Briefly, it was a 100 mM

216   phosphate buffer solution (PBS; 70 g Na_2HPO_4 and 12 g KH_2PO_4 per liter) with the following components

217   in 1 L of deionized water: NH_4Cl (0.41 g); 1 mL of 4 g L^{-1} $FeCl_2$ solution; 10 mL of mineral medium. The

218   mineral media had the composition described by Parameswaran *et al.* [44]: EDTA (0.5 g L^{-1}); $CoCl_2 \bullet 6H_2O$

219   (0.082 g L^{-1}); $CaCl_2 \bullet 2H_2O$ (0.114 g L^{-1}); H_3BO_3 (0.01 g L^{-1}); $Na_2MoO_4 \bullet 2H_2O$ (0.02 g L^{-1}); Na_2SeO_3 (0.001 g L^{-1}

220     $^{-1}$); $Na_2WO_4 \bullet 2H_2O$ (0.01 g L^{-1}); $NiCl_2 \bullet 6H_2O$ (0.02 g L^{-1}); $MgCl_2$ (1.16 g L^{-1}); $MnCl_2 \bullet 4H_2O$ (0.59 g L^{-1}); $ZnCl_2$ (0.05

221   g L^{-1}); $CuSO_4 \bullet 5H_2O$ (0.01 g L^{-1}); $AlK(SO_4)_2$ (0.01 g L^{-1}).

222   After the subsequent current decline, the anolyte was removed and refilled by the same amount of

223   electrolyte (120 mL), this time composed entirely by the synthetic medium added with 7.7 g L^{-1} of sodium

224   acetate. This refill established the end of the acclimation phase and the starting point of the operational

225   period of each system. A schematic overview of the acclimation and operational phases electrolytes is

226   given in Table 2.

ACCLIMATION		OPERATIONAL PERIOD			
A1: Day 0 – Day 17	**A2:** Day 17 – Day 25	**P1:** Day 25 – Day 40	**P2:** Day 40 – Day 58	**P3:** Day 58 – Day 72	**P4:** Day 72 – Day 90
120 mL swine manure	60 mL swine manure + 60 mL synthetic medium	7.7 g L^{-1} CH_3COONa in 120 mL synthethic medium	7.7 g L^{-1} CH_3COONa in 120 mL synthethic medium	7.7 g L^{-1} CH_3COONa in 120 mL synthethic medium	7.7 g L^{-1} CH_3COONa in 120 mL synthethic medium

227   **Table 2**. Timeline and details of each experimental phase.

228 Along the experiment, power curves were periodically recorded with a two-electrode configuration.
229 Before each electrochemical measurement, 1 h equilibration time was found necessary to allow the BES
230 system, disconnected from the data logger, to reach its open circuit potential (OCP). The anode was set
231 as working electrode and the cathode as reference electrode. A linear sweep polarization (v = 0.010 V min^{-1}
232 ^{1}) was recorded from the cell OCP to 10 mV. Power (P) was calculated by $P = I\,V$ and plotted vs current
233 density (j).

2.7 Biofilms visualization by fluorescence microscopy

235 Biofilms growing on both external and internal sides of *e*-BAC bio-cathodes were visualized by
236 fluorescence microscopy. The samples were collected using adhesive tape strips that reproduce the mirror
237 image of the biofilm present in the selected area. The lectin Concanavalin A-Texas Red conjugate (ConA,
238 Invitrogen, Italy) was used to visualize the polysaccharide component of biofilm matrix (extracellular
239 polymeric substances, EPS), whereas the fluorescent nucleic acid stain 4', 6-diamidino-2-phenylindole
240 (DAPI, Sigma-Aldrich srl, Milan, Italy) was used to display biofilm cells. Samples were incubated with 200
241 µg µL^{-1} ConA and 10 µg mL^{-1} DAPI solution in ddH$_2$O at room temperature in the dark for 30 min, and then
242 rinsed. Images were collected using a Leica DM 4000 B microscope equipped with specific filter sets, and
243 a 63X 0.7NA water immersion objective. Digital images acquired using the CoolSNAP CF digital camera
244 (Photometrics Roper Scientific) and elaborated using the ImageJ 1.34s software.

2.8 ICP-MS

246 Inductively coupled plasma mass spectrometry (ICP-MS) was used to measure total contents of single
247 elements in the *e*-BAC at t=0 and t=70 days. Weighted amounts of materials were mineralized by a
248 microwave digestor system (Anton Paar MULTIWAVE-ECO) in Teflon tubes filled with 10 mL of 65% HNO$_3$
249 by applying a one-step temperature ramp (210 °C reached in 10 min and maintained for further 10 min).
250 After 20 min of cooling time, the mineralized samples were transferred in polypropylene test tubes.
251 Solutions of mineralized samples were diluted 1:100 with 0.3 M HNO$_3$ in MILLI-Q water and the
252 concentration of elements was measured by ICP-MS (BRUKER Aurora-M90 ICP-MS). An aliquot of a 2 mg
253 L^{-1} of an internal standard solution (72Ge, 89Y, 159Tb) was added both to samples and calibration curve
254 to give a final concentration of 20 µg L^{-1}. Typical polyatomical analysis interferences were removed by
255 using CRI (Collision-Reaction-Interface) with an H$_2$ flow of 75 mL min^{-1} flown through skimmer cone.

3. Results and discussion

257 *3.1 Rigid and porous cylindrical structure*

258 After the 900 °C-pyrolysis treatment, the materials maintained its structural rigidity and cylindrical shape

259 (Fig. 1). This was the first fundamental requirement fulfilled by this experiment. By sealing its bottom and

260 immersing its external surface in water, the internal surface got wet because of water penetration but

261 without filling the internal part of the cylinder over time. This means that the porous structure of the

262 material was enough to let water pass through it. At the same time, pores volume and diameters were

263 impeding fast flow of the liquid towards the air-exposed side. At the air-water interface, evaporation has

264 time to take place, being evaporation and water flow well balanced. Similar approaches in BES field were

265 developed by other research groups, introducing air-water separators (such as terracotta ref [45]) which

266 had the function of hindering water to flow out rapidly and without introducing too high resistance. The

267 'terracotta' (typical porosity 60-500 nm [3,46]) gets imbibed and acts as porous medium that allows

268 electrolytes mobility. In a previous experiment from our group [33], we employed a ligno-cellulosic

269 biomass (Giant Cane), as separator between electrodes. However, since plant materials underwent partial

270 biodegradation over time, they released elements inside the anolytes. In each of these examples however,

271 the separator was acting as the structural element of the BES. In this experiment we verified that, by direct

272 pyrolysis of the biomass, the cathodic electrode itself is able to give the structure to the BES, without any

273 further separator (and hence resistance) addition.
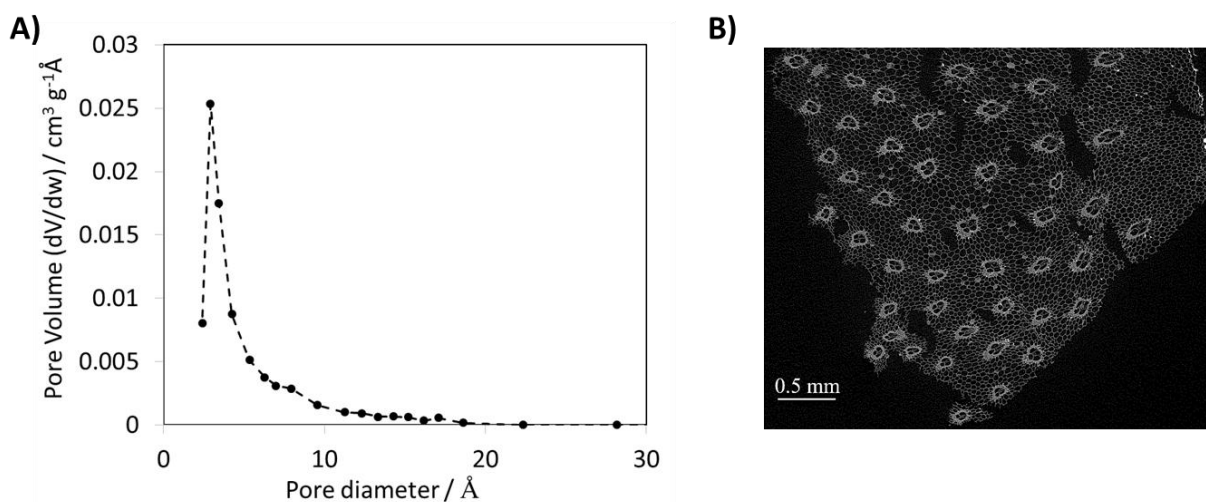
274

275 **Fig. 2** A) Pore size distribution by BJH analysis. B) MicroCT cross-sections of *e*-biochar air-cathode.

276 *e*-BACs underwent N_2 adsorption/desorption, to measure the BET specific surface area (SSA) which was

277 found equal to 114 ± 4 m^2 g^{-1}. Higher specific surface area was hence obtained, with respect to the dry

278 and non-pyrolysed Giant Cane, as reported in the literature by Basso *et al.* (0.7 m^2 g^{-1}) [36]. The same

279   authors also reported the specific surface area value obtained treating Giant Cane stems at 800 °C, a

280   temperature similar to what was used in the present work and they obtained 101 $m^2\,g^{-1}$ [36]. This is in line

281   with the specific surface area measured for *e*-BACs. From the analysis of the porosity, the great part (>

282   95%) of *e*-BAC surface area is comprised in pores with a diameter smaller than 1 nm. Basso *et al.* [36]

283   found similar results for the 800 °C treated sample, with a mean pore radius of about 1.1 nm.

284   Microporosity is therefore the predominant range of pores in the analysed sample, as displayed in Fig. 2A,

285   showing the pore size distribution.

286   The largest pores, in the macroporosity range, are not quantifiable by BJH analysis and a 3D micro-

287   computed tomography was performed in order to evaluate the morphology of the pyrolized sample in

288   the μm range. A sub-volume of 51.44 mm^3 were analyzed containing 74.77 % voids, 25.17 % *e*-BAC matrix

289   and 0.06 % residue of pyrolysis (volume %). In Fig. 2B, a microCT cross section of *e*-BAC is shown. The

290   structure of the vascular bundles is still present after the pyrolysis. From the inner to the outer surface, a

291   continuous accumulation of vascular bundles can be observed resisting greater static stresses in this zone.

292   The bundle fiber thickness is in the range of 15 and 25 μm. These points were confirmed by Rüggeberg *et*

293   *al.* [47], describing the morphological and anatomical features at different structural levels of Giant Cane.

294   The culms are subdivided into nodes and internodes with numerous isolated vascular bundles with

295   enclosing fibre rings embedded in lignified parenchyma further stiffen the culm, as shown in Fig. 2B after

296   the pyrolysis process. The same features were found in the cross section images in the paper by Rüggeberg

297   *et al.* [47].

298   Analyzing the inner surface and volume of the void space, the specific surface area was determined equal

299   to 29 mm^2/mm^3. From the arithmetic mean value of the volume-related surface area of single pores

300   approximated as long cylinders, the equivalent diameter is estimated to be about 38.9 μm. Further, the

301   average particle diameter of pyrolysis residue is to be about 21.9 μm.

302   *3.2. Graphitization degree and electrical conductivity*

303   Another important parameter to be determined for *e*-BACs is its electrical conductivity. Raman

304   spectroscopy is one of the most useful tools to establish the graphitization degree, which correlates with

305   the electrical resistance (and hence the electrical conductivity) [48]. Fig. 3A shows Raman spectra of *e*-

306   BACs which displays the two typical carbon bands: the D band between 1300 and 1400 cm^{-1}, related to

307   vibrations that are forbidden in perfect graphite and become active in the presence of disorder and

308   defects, and the G band between 1500 and 1600 cm^{-1} attributable to in-plane bond-stretching vibrations

309   of trigonally bonded carbon atoms (sp^2 centers)[49]. From the ratio between the D and G peaks intensity,

310   it is possible to discern the presence of disordered/ordered graphene structures affecting the sample
311   conductivity. Usually, upon annealing, the D peak becomes more intense respect to the G one [48]. An
312   increase in the number and size of graphitic clusters is known to translate into an increase in I_D/I_G in
313   amorphous carbons, according to the three-stage model of Ferrari *et al.* [48]. A I_D/I_G, equal to 2.26 was
314   indeed found for the *e*-BAC. This is also coherent with other measurements found in the literature [50].
315   Starting from the acquired spectrum and using the equation provided by Cancado *et al.* [51], 8.46 nm was
316   determined as the crystallite size.
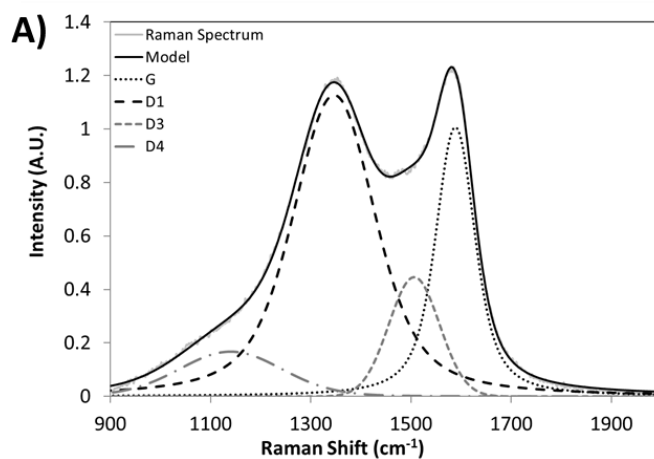
317
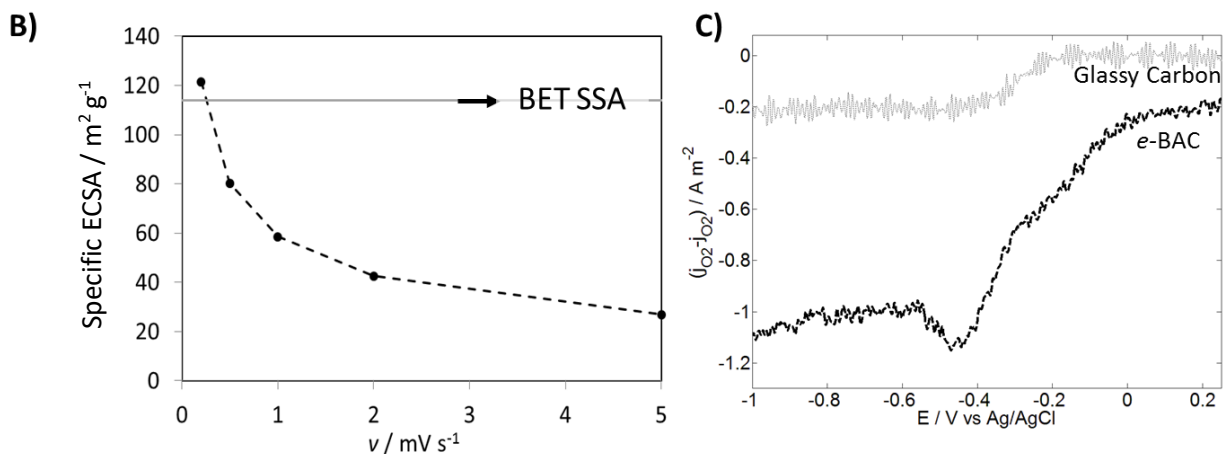
318

319   **Fig. 3** A) Raman spectrum of *e*-biochar air-cathodes. B) specific ECSA determinations. C) ORR cathodic
320   polarization curves.

321   The electrical c of *e*-BACs was measured and compared to other carbon materials in the literature. The
322   method applied in this work on *e*-BACs, resulted in an electrical resistivity value of $8.9 \times 10^{-3} \pm 1 \times 10^{-4} \, \Omega$ m.
323   As expected, this value indicates a higher resistivity with respect to graphite. Graphite is well-known to
324   possess electrical resistivity varying depending on the measurement axes [52,53] and equal to 2.50×10^{-6}

325 - 5.00×10^{-6} Ω m if measured parallel to the basal plane and about 3.00×10^{-3} Ω m if measured

326 perpendicularly to the basal plane [53]. However, the *e*-BACs matrix displays a comparable or lower

327 resistivity, and hence a higher conductivity, as compared to other biochar-based materials, reported in

328 the literature. For instance, resistivity was around 5.15×10^{-3} Ω m for activated carbon [54], 0.98 Ω m for

329 rice straw treated at 800 °C [55].

330 Double layer charging currents were then recorded within the scan rates range between 0.2 mV s^{-1} and 5

331 mV s^{-1}. Higher scan rates avoided the system to reach an electrical charging equilibrium due to the large

332 presence of micropores, hindering ions diffusion inside pores. Fig. 3B shows the values of specific ECSA,

333 calculated at different scan rates. As expected, the real available surface area decreased with increasing

334 scan rates. This is due to the presence of micropores, hindering ions diffusion inside the material, hence

335 unable to reach an electrical charging equilibrium if the potential variation over time is too fast.

336 The highest value of specific ECSA was obtained by the lowest scan rate (0.2 mV s^{-1}) and this value is in

337 fact very similar to the BET specific surface area (114 ± 4 m^2 g^{-1}). This means that the electric surface area

338 corresponds to the BET surface area only with scan rates equal or lower than 0.2 mV s^{-1}.

339 In general, characterization of carbon/solution interfaces is more complex than that of metals [56]. As

340 explained by equation (2), the weak point of the calculation is relative to the choice of the appropriate C_{ref}

341 value. An improper choice of C_{ref} might drive to unreliable calculations of real electrical SSA. Pore

342 accessibility is the most critical point dealing with capacitance of carbon materials [56]. Other problems

343 arise due to the fact that carbons are not ideally polarizable, as noble metals (*e.g.* Hg) are. This is

344 attributable to surface oxidation or intercalation processes [56].

345 Here, the chosen reference value of specific capacity was C_{ref} = 9.57 μF cm^{-2}, for similarity to materials

346 with similar characteristics [42]. This value refers to Vulcan XC72, a material with similar BET surface area

347 (131.6 m^2 g^{-1}), as compared to *e*-BACs (114 ± 4 m^2 g^{-1}). Also, the specific mass capacitance of this reference

348 material (12.6 μF g^{-1}) is very close to that one calculated for *e*-BACs sample at the lowest scan rate (11.6 μF

349 g^{-1}).

350 *3.3. ORR electrocatalytic activity*

351 The electrocatalytic properties of *e*-BAC towards the ORR were investigated. Fig. 3C shows the ORR

352 polarization curves for a glassy carbon electrode (GC) covered by the *e*-BAC powder. For comparison, the

353 figure also reports a second polarization curve for the bare GC electrode, recorded in the same conditions.

354 Cathodic limiting current densities (normalized by the geometric area of the GC electrode) were equal to

355 -1 A m^{-2} and -0.2 A m^{-2} for *e*-BAC and GC, respectively. The presence of the *e*-BAC catalyst not only

356 enhanced the limiting currents, but also shifted the onset potential from -0.200 V vs Ag/AgCl ($E_{1/2}$=-0.3 V

357 vs Ag/AgCl) to cathodic value of -0.020 V vs Ag/AgCl ($E_{1/2}$=-0.2 V vs Ag/AgCl).

358 As compared to other catalysts used in the literature to maximize current generation in fuel cells or

359 microbial fuel cells, *e*-BAC produced relatively low ORR currents displaying higher overpotentials. For

360 example, Liu *et al.* doped graphene-based cathodes with nitrogen heteroatoms [57]: the onset potential

361 was found to be 200 mV less cathodic, compared to *e*-BAC, at the same pH conditions. Also, reduction

362 currents were higher by one order of magnitude. Many other examples in the literature were presented

363 in the direction of electrocatalytic activity enhancement without any precious metal content [58]. The

364 kinetics characteristics of these kind of carbon towards ORR are better [58] compared to what obtained

365 in this work, nevertheless, the production of these carbon-based catalysts is usually time-consuming.

366 Moreover, synthetic or costly reactants are employed. Instead, in this work, despite lower electrocatalytic

367 performance were achieved, *e*-BACs were fabricated with facile pyrolysis of Giant Cane stalks, without

368 any kind of pre- or post-treatment. This aspect is advantageous in terms of simplicity in electrodes

369 preparation and a potential greater suitability for applications in natural environments, for processes such

370 as biodegradation of pollutants, where even a slow electrocatalysis could be enough.

371 *3.4 e-biochar air-exposed bio-cathodes performances in BES*

372 *e*-BACs were tested as potential hosts of electroactive biofilm communities, as air-exposed bio-cathodes.

373 After assembling *e*-BACs in simple BES architectures as shown in Fig. 1, currents were monitored over

374 time. The current density trends, reported in Fig. 4A, showed a standard deviation between the triplicates

375 of about 5%. During a first acclimation period (A1), the anolyte was totally composed by swine manure as

376 inoculum. After an initial and expected delay, around day 12 the systems started producing current, up to

377 a maximum of about 100 mA m^{-2}. In a second acclimation period (A2), during which half of the anolyte

378 was substituted by the synthetic medium, the systems produced less current compared to the previous

379 cycle (with a maximum of about 70 mA m^{-2}), and this might be due to the sudden replacement of the

380 medium of the bacteria colonizing the electrodes which still needed to adapt to the new environment.

381 After the A2 phase, the real operational period (P1) began, characterized by the whole presence of the

382 synthetic medium as the anolyte and sodium acetate (7.7 g L^{-1}) as the standard feed for bacteria. During

383 cycle P1 the current production was comparable to the last cycle of acclimation. This, once again, could

384 be related to the last sudden replacement of the bacteria environment. In a second acetate batch cycle

385 (P2) in fact the recorded current densities are higher and equal to about 130 mA m^{-2}. However, during the

386 next cycles P3 and P4, the systems were not further able to produce current higher as before, showing a

14

387 maximum current densities of 25 mA m^{-2} and 15 mA m^{-2} in cycles P3 and P4, respectively. Also power

388 densities were much lower (less than 5 mW m^{-2}) as compared to the starting operational period of the

389 system, as reported in Fig. 4B.

390

396
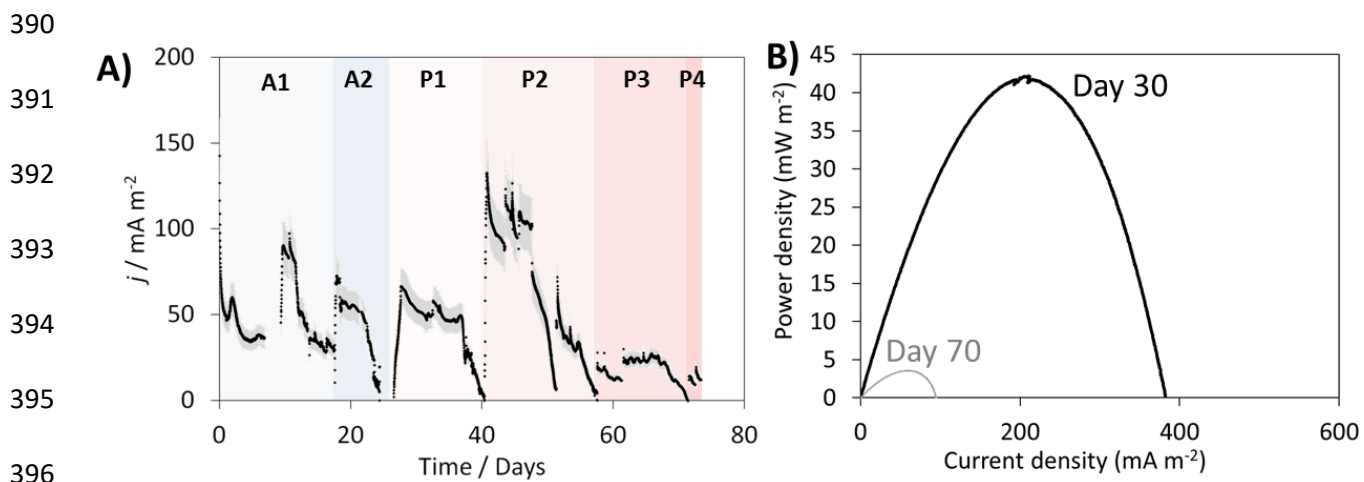
397 **Fig. 4**. A) Trends of current density obtained by BES, equipped with *e*-biochar air-cathode. Black line shows

398 the average trend, the grey region shows the standard deviation of triplicate experiments. In acclimation

399 batch-cycles (A1, A2) swine manure was fed to the anodic chamber; in successive batch cycles (P1-P4)

400 sodium acetate (7.7 g L^{-1}) was used as carbon source. B) Power density curves at day 30 and at day 70.

401 Representative biofilm structures observed for the *e*-BAC bio-cathode are presented in Fig. 5. The images

402 display microbial colonization of the water-side of the cathode (Fig. 5 A-B), exposed to bacteria. The

403 biofilm is characterized by a marked structural heterogeneity, showing several morphotypes of

404 microorganisms assembled in dense clusters. The lectin-binding analysis combined with fluorescence

405 microscopy revealed the presence of extracellular polymeric substances glycol-conjugates (*i.e.*

406 polysaccharides, including those ones covalently linked to proteins and/or lipids) in all the samples

407 colonizing the external side of an *e*-BAC.

408 By contrast, the inner surface of an *e*-BAC, exposed to air was poorly colonized, showing few coccoid

409 morphotypes organized in small assemblages. No signal derived from the lectin-binding analysis was

410 detected, indicating the absence of an extracellular matrix typical of mature and well structured biofilms

411 (Fig. 5C).
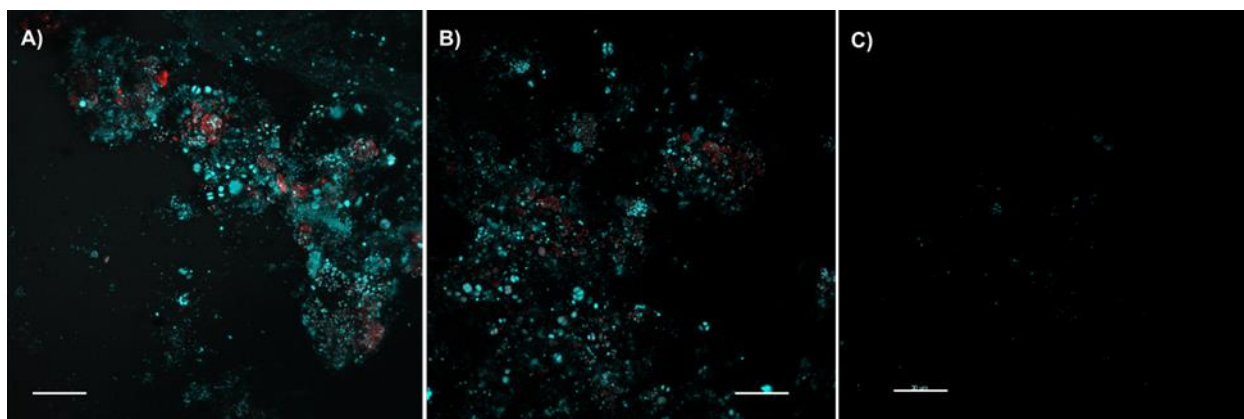
Fig. 5. Fluorescent images of the biofilms colonizing the water-side (panel A-B) and air-side (panel C) of a *e*-biochar air-exposed bio-cathode. Color key: Biofilm cells, blue (DAPI); EPS matrix, red (ConA). Scale bars 30 μm.

These results indicate that the dimension of pores of the *e*-biochar impeded the passage of microorganisms from the anolyte towards the air-side. In this region, the electroactive sites of *e*-BAC exposed to air catalyse the ORR with an electroactivity that was previously investigated by electrochemical reduction polarization curves measured on *e*-BAC powder (Fig. 3B). However, it cannot be excluded that bacteria, colonizing the water-side of the cathode facing the anolyte, take part in the cathodic oxygen reduction reaction, being in contact with a region where oxygen is likely present, even if at low concentration. *e*-BAC cylinder could be in fact able to diffuse O_2 throughout its thickness, until it reaches the microorganisms. Furthermore, the reduced products from the metabolism of bacteria, such as sulphides, could be able to sustain a chain of cathodic reactions diffusing through the cathode porosity. These aspects that characterized the electrochemical behavior of air-breathing carbon bio-cathode, as discussed in previous works [10,46,59], deserve further investigations and detailed studies.

3.5 Possible applications of e-biochar air-exposed bio-cathodes

Power density curves (Fig. 4B) report maximum of about 40 mW m^{-2}, recorded at day 30, during the plateau reached under feeding condition. Similar values were obtained in low-tech BES, *e.g.* with Giant Cane stalk or terracotta are employed as air-water separators, using carbon cloth-based electrodes [33,46]. In general, higher-tech microbial fuel cells aimed at energy harvesting in the literature achieve higher current and power densities, as compared to the *e*-BAC [60,61]. Further work would be needed to optimize abiotic ORR reactions, in the direction of introducing more active electrocatalytic centers and increase the ECSA and [62], in parallel, promote microbial colonization of *e*-BAC [63].

435 However, energy harvesting and maximizing power densities might not be the main goal in many
436 applications of *e*-BACs. For example, terracotta-based microbial fuel cells systems were utilized by Gajda
437 *et al.* as self- powered wastewater electrolyser for electrocoagulation of heavy metals, caustic production
438 at cathode (pH > 10) and CO_2 sequestration [64]. They also observed how current generation in cylindrical
439 terracotta microbial fuel cells contributed to generate an electro-osmotic drag and reported catholyte
440 formation (attributed to water transport) in proportion to power performance [65]. pH increase was
441 demonstrated to be responsible of inorganic salts deposition (*e.g* carbonates precipitation) [66] and
442 accumulation as a layer between the cathode and the biofilm, thus preventing charge transfer processes.
443 Here, the relatively low power density (Fig. 4B) was sufficient to generate an electrical field, driving ions
444 migration at cathode and inducing salts deposition phenomena (likely thanks also to locally increased pH
445 conditions [67]). The observed decrease in currents and maximum power density (Fig. 4) fit with the
446 hypothesis of salts deposition phenomena. After 70 operational days, *e*-BAC appeared covered by salts
447 deposits (Fig. 6). The materials were analyzed by SEM microscopy, ICP-MS and BET, to detect the presence
448 and the amount of elements that underwent deposition over time. In SEM images (Fig. 6A), the structure
449 of the pristine, pyrolysed Giant Cane is clearly visible. In Fig 6B, the presence of crystals of different shapes,
450 deposited on the external side of the *e*-BAC cylinder, facing the wastewater is massive.
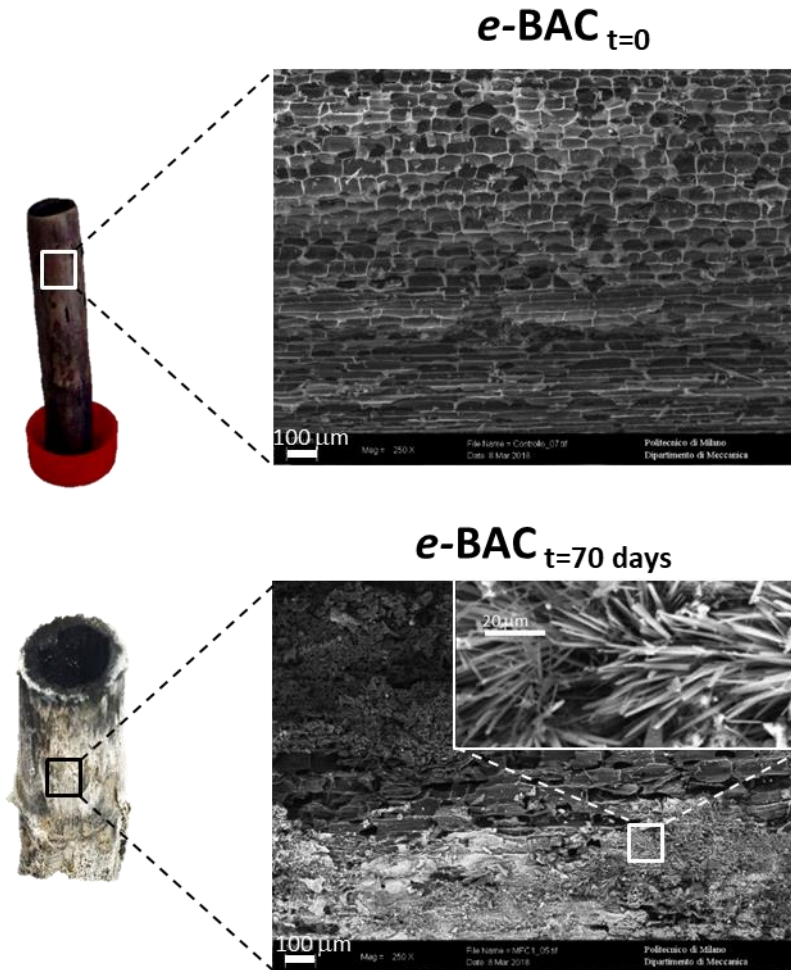
451

452 Fig.6 - Pictures and SEM images of the *e*-BAC at t=0 and after 70 days operation in BES.

453

454 From ICP-MS, several elements originally contained in the synthetic wastewater were retrieved on the *e*-

455 BAC. Na content in the solid material increased by 79 folds, as compared its initial value. Ca and P

456 increased by 1.3 and 5 folds, respectively. Nitrogen was not measured in this work and would deserve

457 particular attentions in future experiments.

458 Salts deposition likely caused a decrease in the availability of the electroactive sites on the cathode and

459 clogged its porous texture. Accordingly, BET surface area measured at day 70 was under the instrumental

460 detection limit. Even if the precise value could not be measured, the *e*-BAC material underwent a decrease

461 of at least two-orders of magnitude in available surface area, along the 70-days test.

462 The phenomenon of salts deposition in air-exposed biocathodes was recently documented in the

463 literature by Santini *et al.* [14]. Together with carbonates, other salts are likely to deposit (such as struvite

464 and other salts containing macro- e micro-nutrients previously dissolved or suspended in the wastewater).

465 This aspect could be of great interest for environmental application such as nutrients recovery in agro-
466 food systems. When salts deposition clogs the cathode, impeding charge transfer processes, the *e*-biochar
467 cathode could be substituted with a new one. The *e*-biochar enriched of plant nutrients might be recycled
468 directly as agricultural soil conditioner. Biochar is widely considered as a soil-fertility promoter and a way
469 to achieve long-term carbon storage [68]. Thereby, salts deposition phenomena on *e*-BACs can be
470 considered as an advantage, to maximize nutrients recovery from wastewater in agro-food systems. On
471 the other hand, future studies in this field should consider to detect possible contaminants (*e.g.* heavy
472 metals, antibiotics, etc.) that might be contained in the treated wastewater.

473 **4. CONCLUSIONS**

474 *e*-biochar was prepared by controlled pyrolysis of Giant Cane stalks and characterized for physico-
475 chemical and electrochemical features. The structure and shape of Giant Cane were maintained after the
476 pyrolysis process and it was advantageous in building cylindrical and self-structured air-exposed
477 biocathode. This new material might reduce the need of technological materials in BES, and the cost of
478 bioelectrodes, especially for some applications. The fragility of the *e*-BAC structure represents an actual
479 drawback which needs an improvement, this might be overcome by addition of compounds that anyway
480 must not decrease the conductivity and properties of the overall matrix. The step forward would be to
481 work on the structure and prepare composite materials through which the thickness would result
482 increased, together with an enhanced rigidity. Despite improvements would be needed to achieve
483 current/power densities of more technological and optimized materials, the *e*-biochar could open new
484 frontiers in BES' architectures, where energy harvesting is not the main goal. The produced currents
485 induced ions migration and salts deposition, clogging porous texture and enriching *e*-biochar of minerals.
486 This approach goes into the direction of achieving fully-recyclable BES architectures, directly reusable to
487 produce soil fertilizers. In parallel, further developments are needed to design bigger scale
488 biocathodes/anodes and to optimize their properties and performances, according to the desired
489 application.

490 **AKNOWLEDGEMENTS**

495 **REFERENCES**

496 [1]   Wei J, Liang P, Huang X. Recent progress in electrodes for microbial fuel cells. Bioresour Technol
497   2011;102:9335–44. doi:10.1016/j.biortech.2011.07.019.

498 [2]   Zhou M, Chi M, Luo J, He H, Jin T. An overview of electrode materials in microbial fuel cells. J
499   Power Sources 2011;196:4427–35. doi:10.1016/j.jpowsour.2011.01.012.

500 [3]   Santoro C, Artyushkova K, Gajda I, Babanova S, Serov A, Atanassov P, et al. Cathode materials for
501   ceramic based microbial fuel cells (MFCs). Int J Hydrogen Energy 2015;40:14706–15.
502   doi:10.1016/j.ijhydene.2015.07.054.

503 [4]   Kumar GG, Sarathi VGS, Nahm KS. Recent advances and challenges in the anode architecture and
504   their modifications for the applications of microbial fuel cells. Biosens Bioelectron 2013;43:461–
505   75. doi:10.1016/j.bios.2012.12.048.

506 [5]   You J, Santoro C, Greenman J, Melhuish C, Cristiani P, Li B, et al. Micro-porous layer (MPL)-based
507   anode for microbial fuel cells. Int J Hydrogen Energy 2014;39:21811–8.
508   doi:10.1016/j.ijhydene.2014.07.136.

509 [6]   Santoro C, Lei Y, Li B, Cristiani P. Power generation from wastewater using single chamber
510   microbial fuel cells (MFCs) with platinum-free cathodes and pre-colonized anodes. Biochem Eng J
511   2012;62:8–16. doi:10.1016/j.bej.2011.12.006.

512 [7]   Santoro C, Agrios A, Pasaogullari U, Li B. Effects of gas diffusion layer (GDL) and micro porous
513   layer (MPL) on cathode performance in microbial fuel cells (MFCs). Int J Hydrogen Energy
514   2011;36:13096–104. doi:10.1016/j.ijhydene.2011.07.030.

515 [8]   Srikanth S, Pant D, Dominguez-Benetton X, Genné I, Vanbroekhoven K, Vermeiren P, et al. Gas
516   Diffusion Electrodes Manufactured by Casting Evaluation as Air Cathodes for Microbial Fuel Cells
517   (MFC). Materials (Basel) 2016;9:601. doi:10.3390/ma9070601.

518 [9]   Terayama Y, Haji T, Furukawa S, Nomura M, Nishihara M, Lyth SM, et al. Carbon black / PTFE
519   composite hydrophobic gas diffusion layers for a water-absorbing porous electrolyte electrolysis
520   cell. Int J Hydrogen Energy 2018;43:2018–25. doi:10.1016/J.IJHYDENE.2017.12.045.

521 [10] Rago L, Cristiani P, Villa F, Zecchin S, Colombo A, Cavalca L, et al. Influences of dissolved oxygen
522   concentration on biocathodic microbial communities in microbial fuel cells. Bioelectrochemistry

523 2017;116:39–51. doi:10.1016/j.bioelechem.2017.04.001.

[11] Guerrini E, Grattieri M, Faggianelli A, Cristiani P, Trasatti S. PTFE effect on the electrocatalysis of the oxygen reduction reaction in membraneless microbial fuel cells. Bioelectrochemistry 2015;106:240–7. doi:10.1016/j.bioelechem.2015.05.008.

[12] Fan Y, Han S-K, Liu H, Keller J, Buisman CJ, Rittmann BE, et al. Improved performance of CEA microbial fuel cells with increased reactor size. Energy Environ Sci 2012;5:8273. doi:10.1039/c2ee21964f.

[13] Katuri KP, Kalathil S, Ragab A, Bian B, Alqahtani MF, Pant D, et al. Dual-Function Electrocatalytic and Macroporous Hollow-Fiber Cathode for Converting Waste Streams to Valuable Resources Using Microbial Electrochemical Systems. Adv Mater 2018:1707072. doi:10.1002/adma.201707072.

[14] Santini M, Marzorati S, Fest-Santini S, Trasatti S, Cristiani P. Carbonate scale deactivating the biocathode in a microbial fuel cell. J Power Sources 2017;356. doi:10.1016/j.jpowsour.2017.02.088.

[15] Zhang F, Pant D, Logan BE. Long-term performance of activated carbon air cathodes with different diffusion layer porosities in microbial fuel cells. Biosens Bioelectron 2011;30:49–55. doi:10.1016/J.BIOS.2011.08.025.

[16] Pant D, Van Bogaert G, Porto-Carrero C, Diels L, Vanbroekhoven K. Anode and cathode materials characterization for a microbial fuel cell in half cell configuration. Water Sci Technol 2011;63:2457. doi:10.2166/wst.2011.217.

[17] Rossi R, Yang W, Zikmund E, Pant D, Logan BE. In situ biofilm removal from air cathodes in microbial fuel cells treating domestic wastewater. Bioresour Technol 2018;265:200–6. doi:10.1016/J.BIORTECH.2018.06.008.

[18] Cheng S, Liu H, Logan BE. Increased performance of single-chamber microbial fuel cells using an improved cathode structure. Electrochem Commun 2006;8:489–94. doi:10.1016/j.elecom.2006.01.010.

[19] Kim JR, Cheng S, Oh S-E, Logan BE. Power Generation Using Different Cation, Anion, and Ultrafiltration Membranes in Microbial Fuel Cells. Environ Sci Technol 2007;41:1004–9.

21

551   doi:10.1021/es062202m.

552   [20] Franks AE, Nevin KP. Microbial fuel cells, a current review. Energies 2010;3:899–919.

553   doi:10.3390/en3050899.

554   [21] Rismani-Yazdi H, Carver SM, Christy AD, Tuovinen OH. Cathodic limitations in microbial fuel cells:

555   An overview. J Power Sources 2008;180:683–94. doi:10.1016/j.jpowsour.2008.02.074.

556   [22] Ioannidou O, Zabaniotou A. Agricultural residues as precursors for activated carbon production-A

557   review. Renew Sustain Energy Rev 2007;11:1966–2005. doi:10.1016/j.rser.2006.03.013.

558   [23] Yuan Y, Liu T, Fu P, Tang J, Zhou S. Conversion of sewage sludge into high-performance

559   bifunctional electrode materials for microbial energy harvesting. J Mater Chem A 2015;3:8475–

560   82. doi:10.1039/C5TA00458F.

561   [24] Qian K, Kumar A, Zhang H, Bellmer D, Huhnke R. Recent advances in utilization of biochar. Renew

562   Sustain Energy Rev 2015;42:1055–64. doi:10.1016/j.rser.2014.10.074.

563   [25] Huggins T, Wang H, Kearns J, Jenkins P, Ren ZJ. Biochar as a sustainable electrode material for

564   electricity production in microbial fuel cells. Bioresour Technol 2014;157:114–9.

565   doi:10.1016/j.biortech.2014.01.058.

566   [26] Chen S, Tang J, Fu L, Yuan Y, Zhou S. Biochar improves sediment microbial fuel cell performance

567   in low conductivity freshwater sediment n.d. doi:10.1007/s11368-016-1452-z.

568   [27] Cruz Viggi C, Simonetti S, Palma E, Pagliaccia P, Braguglia C, Fazi S, et al. Enhancing methane

569   production from food waste fermentate using biochar: the added value of electrochemical

570   testing in pre-selecting the most effective type of biochar. Biotechnol Biofuels 2017;10:303.

571   doi:10.1186/s13068-017-0994-7.

572   [28] Chen S, Rotaru A-E, Shrestha PM, Malvankar NS, Liu F, Fan W, et al. Promoting interspecies

573   electron transfer with biochar. Sci Rep 2014;4:5019. doi:10.1038/srep05019.

574   [29] Ma M, You S, Wang W, Liu G, Qi D, Chen X, et al. Biomass-Derived Porous Fe 3 C/Tungsten

575   Carbide/Graphitic Carbon Nanocomposite for Efficient Electrocatalysis of Oxygen Reduction. ACS

576   Appl Mater Interfaces 2016;8:32307–16. doi:10.1021/acsami.6b10804.

577   [30] Huggins TM, Pietron JJ, Wang H, Ren ZJ, Biffinger JC. Graphitic biochar as a cathode

578   electrocatalyst support for microbial fuel cells. Bioresour Technol 2015;195:147–53.

579   doi:10.1016/j.biortech.2015.06.012.

580 [31] Yuan H, Deng L, Qi Y, Kobayashi N, Tang J. Nonactivated and activated biochar derived from
581   bananas as alternative cathode catalyst in microbial fuel cells. ScientificWorldJournal
582   2014;2014:832850. doi:10.1155/2014/832850.

583 [32] Chen Q, Pu W, Hou H, Hu J, Liu B, Li J, et al. Activated Microporous-Mesoporous Carbon Derived
584   from Chestnut Shell as a Sustainable Anode Material for High Performance Microbial Fuel Cells.
585   Elsevier Ltd; 2017. doi:10.1016/j.biortech.2017.09.086.

586 [33] Marzorati S, Schievano A, Colombo A, Lucchini G, Cristiani P. Ligno-cellulosic materials as air-
587   water separators in low-tech microbial fuel cells for nutrients recovery. J Clean Prod
588   2018;170:1167–76. doi:10.1016/J.JCLEPRO.2017.09.142.

589 [34] Corno L, Pilu R, Adani F. Arundo donax L.: A non-food crop for bioenergy and bio-compound
590   production. Biotechnol Adv 2014;32:1535–49. doi:10.1016/j.biotechadv.2014.10.006.

591 [35] Valli F, Trebbi D, Zegada-Lizarazu W, Monti A, Tuberosa R, Salvi S. In vitro physical mutagenesis of
592   giant reed (Arundo donax L.). GCB Bioenergy 2017;9:1380–9. doi:10.1111/gcbb.12458.

593 [36] Basso MC, Cerrella EG, Buonomo EL, Bonelli PR, Cukierman AL. Thermochemical Conversion of
594   Arundo Donax into Useful Solid Products. Energy Sources 2005;27:1429–38.
595   doi:10.1080/009083190523280.

596 [37] Jeguirim M, Trouvé G. Pyrolysis characteristics and kinetics of Arundo donax using
597   thermogravimetric analysis. Bioresour Technol 2009;100:4026–31.
598   doi:10.1016/j.biortech.2009.03.033.

599 [38] Longhi M, Marzorati S, Checchia S, Sacchi B, Santo N, Zaffino C, et al. Sugar-based catalysts for
600   oxygen reduction reaction. Effects of the functionalization of the nitrogen precursors on the
601   electrocatalytic activity. Electrochim Acta 2016. doi:10.1016/j.electacta.2016.11.036.

602 [39] Santini M, Guilizzoni M, Fest-Santini S. X-ray computed microtomography for drop shape analysis
603   and contact angle measurement. J Colloid Interface Sci 2013;409:204–10.
604   doi:10.1016/J.JCIS.2013.06.036.

605 [40] Lukaszewski M, Soszko M, Czerwiński A. Electrochemical methods of real surface area
606   determination of noble metal electrodes - an overview. Int J Electrochem Sci 2016;11:4442–69.

607 doi:10.20964/2016.06.71.

608 [41] Du F, Yu D, Dai L, Ganguli S, Varshney V, Roy AK. Preparation of Tunable 3D Pillared Carbon
609   Nanotube Graphene Networks for High Performance Capacitance. Chem Mater 2011:4810–6.
610   doi:10.1021/cm2021214.

611 [42] Capacitance limits of high surface area activated carbons for double layer capacitors. Carbon N Y
612   2005;43:1303–10. doi:10.1016/J.CARBON.2005.01.001.

613 [43] Rago L, Guerrero J, Baeza JA, Guisasola A. 2-Bromoethanesulfonate degradation in
614   bioelectrochemical systems. Bioelectrochemistry 2015;105:44–9.
615   doi:10.1016/j.bioelechem.2015.05.001.

616 [44] Parameswaran P, Torres CI, Lee HS, Krajmalnik-Brown R, Rittmann BE. Syntrophic interactions
617   among anode respiring bacteria (ARB) and non-ARB in a biofilm anode: Electron balances.
618   Biotechnol Bioeng 2009;103:513–23. doi:10.1002/bit.22267.

619 [45] Pasternak G, Greenman J, Ieropoulos I. Comprehensive Study on Ceramic Membranes for Low-
620   Cost Microbial Fuel Cells. ChemSusChem 2015:88–96. doi:10.1002/cssc.201501320.

621 [46] Rago L, Zecchin S, Marzorati S, Goglio A, Cavalca L, Cristiani P, et al. A study of microbial
622   communities on terracotta separator and on biocathode of air breathing microbial fuel cells.
623   Bioelectrochemistry 2018;120:18–26. doi:10.1016/J.BIOELECHEM.2017.11.005.

624 [47] Ruggeberg M, Burgert I, Speck T. Structural and mechanical design of tissue interfaces in the
625   giant reed Arundo donax. J R Soc Interface 2010;7:499–506. doi:10.1098/rsif.2009.0273.

626 [48] Ferrari AC, Robertson J. Interpretation of Raman spectra of disordered and amorphous carbon.
627   Phys Rev B 2000;61:14095–107. doi:10.1103/PhysRevB.61.14095.

628 [49] Marzorati S, Vasconcelos JM, Ding J, Longhi M, Colavita PE, Carrette L, et al. Template-free
629   ultraspray pyrolysis synthesis of N/Fe-doped carbon microspheres for oxygen reduction
630   electrocatalysis. J Mater Chem A 2015;3:18920–7. doi:10.1039/C5TA02570B.

631 [50] Bernard S, Beyssac O, Benzerara K, Findling N, Tzvetkov G, Brown GE. XANES, Raman and XRD
632   study of anthracene-based cokes and saccharose-based chars submitted to high-temperature
633   pyrolysis. Carbon N Y 2010;48:2506–16. doi:10.1016/j.carbon.2010.03.024.

634 [51] Caṇado LG, Takai K, Enoki T, Endo M, Kim YA, Mizusaki H, et al. General equation for the

635 determination of the crystallite size la of nanographite by Raman spectroscopy. Appl Phys Lett
636 2006;88:1998–2001. doi:10.1063/1.2196057.

637 [52] Deprez N, McLachlan DS. The analysis of the electrical conductivity of graphite conductivity of
638 graphite powders during compaction. J Phys D Appl Phys 1988;21:101–7. doi:10.1088/0022-
639 3727/21/1/015.

640 [53] Pierson HO. Handbook of Carbon, Graphite, Diamond and Fullerenes. Handb Carbon, Graph Diam
641 Fullerenes 1993:25–69. doi:http://dx.doi.org/10.1016/B978-0-8155-1339-1.50008-6.

642 [54] Barroso-Bogeat A, Alexandre-Franco M, Fernández-González C, Macías-García A, Gómez-Serrano
643 V. Electrical conductivity of activated carbon–metal oxide nanocomposites under compression: a
644 comparison study. Phys Chem Chem Phys 2014;16:25161–75. doi:10.1039/C4CP03952A.

645 [55] Adinaveen T, Vijaya JJ, Kennedy LJ. Comparative Study of Electrical Conductivity on Activated
646 Carbons Prepared from Various Cellulose Materials. Arab J Sci Eng 2016;41:55–65.
647 doi:10.1007/s13369-014-1516-6.

648 [56] 9.3.Double layer capacitance of carbon.pdf n.d.

649 [57] Liu Y, Liu H, Wang C, Hou S-X, Yang N. Sustainable Energy Recovery in Wastewater Treatment by
650 Microbial Fuel Cells: Stable Power Generation with Nitrogen-doped Graphene Cathode. Environ
651 Sci Technol 2013;47:13889–95. doi:10.1021/es4032216.

652 [58] Kodali M, Santoro C, Herrera S, Serov A, Atanassov P. Bimetallic platinum group metal-free
653 catalysts for high power generating microbial fuel cells. J Power Sources 2017;366:18–26.
654 doi:10.1016/j.jpowsour.2017.08.110.

655 [59] Cristiani P, Carvalho ML, Guerrini E, Daghio M, Santoro C, Li B. Cathodic and anodic biofilms in
656 Single Chamber Microbial Fuel Cells. Bioelectrochemistry 2013;92:6–13.
657 doi:10.1016/j.bioelechem.2013.01.005.

658 [60] Nguyen MT, Mecheri B, Iannaci A, D'Epifanio A, Licoccia S. Iron/Polyindole-based Electrocatalysts
659 to Enhance Oxygen Reduction in Microbial Fuel Cells. Electrochim Acta 2016;190:388–95.
660 doi:10.1016/j.electacta.2015.12.105.

661 [61] Cristiani P, Carvalho ML, Guerrini E, Daghio M, Santoro C, Li B. Cathodic and anodic biofilms in
662 Single Chamber Microbial Fuel Cells. Bioelectrochemistry 2013;92:6–13.

663   doi:10.1016/j.bioelechem.2013.01.005.

664   [62]   Ruiz-Rosas R, Valero-Romero MJ, Salinas-Torres D, Rodríguez-Mirasol J, Cordero T, Morallón E, et
665   al. Electrochemical Performance of Hierarchical Porous Carbon Materials Obtained from the
666   Infiltration of Lignin into Zeolite Templates. ChemSusChem 2014;7:1458–67.
667   doi:10.1002/cssc.201301408.

668   [63]   Strelko V., Kuts V., Thrower P. On the mechanism of possible influence of heteroatoms of
669   nitrogen, boron and phosphorus in a carbon matrix on the catalytic activity of carbons in electron
670   transfer reactions. Carbon N Y 2000;38:1499–503. doi:10.1016/S0008-6223(00)00121-4.

671   [64]   Gajda I, Stinchcombe A, Greenman J, Melhuish C, Ieropoulos I. Microbial fuel cell e A novel self-
672   powered wastewater electrolyser for electrocoagulation of heavy metals 2016.
673   doi:10.1016/j.ijhydene.2016.06.161.

674   [65]   Gajda I, Greenman J, Melhuish C, Santoro C, Li B, Cristiani P, et al. Water formation at the
675   cathode and sodium recovery using Microbial Fuel Cells (MFCs). Sustain Energy Technol
676   Assessments 2014;7:187–94. doi:10.1016/j.seta.2014.05.001.

677   [66]   Santini M, Marzorati S, Fest-Santini S, Trasatti S, Cristiani P. Carbonate scale deactivating the
678   biocathode in a microbial fuel cell. J Power Sources 2017;356:400–7.
679   doi:10.1016/j.jpowsour.2017.02.088.

680   [67]   Gajda I, Greenman J, Melhuish C, Santoro C, Li B, Cristiani P, et al. Electro-osmotic-based
681   catholyte production by Microbial Fuel Cells for carbon capture. Water Res 2015.
682   doi:10.1016/j.watres.2015.08.014.

683   [68]   Woolf D, Amonette JE, Street-Perrott FA, Lehmann J, Joseph S. Sustainable biochar to mitigate
684   global climate change. Nat Commun 2010;1:1–9. doi:10.1038/ncomms1053.

685